Atmos. Chem. Phys., 26, 15721–15733, 2026
https://doi.org/10.5194/acp-26-15721-2026
© Author(s) 2026. This work is distributed under
the Creative Commons Attribution 4.0 License.

Atmospheric Chemistry and Physics
Open Access
EGU

Research article

Organic condensation derived from different volatility parameterizations and its implications for ambient nanoparticle growth

Chuang Li[1], Runlong Cai[1,2,3], Zexin Chen[1], Gan Yang[1], Feilin Zhao[1], Yueyang Li[1], Jingyu An[4], Qiwen Sun[1], Sijia Yin[1], Shimeng Xu[1], Yiliang Liu[5], Yixi Ma[1], Douglas Worsnop[6], Lei Yao[1], and Lin Wang[1,2,3,7]

[1]Shanghai Key Laboratory of Air Quality and Environmental Health, Department of Environmental Science & Engineering, Fudan University, Shanghai, 200438, China
[2]IRDR ICoE on Risk Interconnectivity and Governance on Weather/Climate Extremes Impact and Public Health, Fudan University, Shanghai, 200438, China
[3]National Observations and Research Station for Wetland Ecosystems of the Yangtze Estuary, Shanghai, China
[4]Key Laboratory of Formation and Prevention of Urban Air Pollution Complex, Ministry of Ecology and Environment, Shanghai Academy of Environmental Sciences, Shanghai, 200233, China
[5]Key Laboratory of Reservoir Aquatic Environment of CAS, Chongqing Institute of Green and Intelligent Technology, Chinese Academy of Sciences, Chongqing, 400714, China
[6]Aerodyne Research Inc., Billerica, MA 01821, USA
[7]Shanghai Institute of Pollution Control and Ecological Security, Shanghai, 200092, China

Correspondence: Lei Yao (lei_yao@fudan.edu.cn) and Lin Wang (lin_wang@fudan.edu.cn)

Received: 2 June 2026 – Discussion started: 21 July 2026
Revised: 29 October 2026 – Accepted: 30 October 2026 – Published: 9 November 2026

Abstract. Atmospheric new particle formation (NPF) supplies up to half of global cloud condensation nuclei, yet the growth of sub-15 nm nanoparticles – the stage most vulnerable to scavenging – remains poorly constrained, largely because the volatility of oxygenated organic molecules (OOMs) is highly uncertain. Using a purpose-built laminar flow reactor that isolates particle–particle coagulation from OOM condensation, we show that six of seven widely used OOM volatility parameterizations substantially overestimate nanoparticle growth rates, with the largest bias under the high-NO_x conditions. A recent parameterization constrained by ambient organic aerosol volatility reproduces our laboratory observations across diverse OOM precursors, seed sizes (3–5 nm), and NO_x regimes. By applying this laboratory-validated framework to NPF events at Lake Tai, China, in summer 2023, OOM and H_2SO_4 condensation explain about 53 % of the observed 3–15 nm growth rate, rising to roughly 86 % at the upper bound of the estimated uncertainty in OOM concentrations. This residual is consistent with, but not uniquely attributable to, processes absent from the present framework: incomplete instrumental coverage of condensable vapours, uncertainties in the measured size distributions and growth rates, and simplifications within the growth model may each contribute, and a box-model estimate indicates that heterogeneous gas–particle reactions could account for a substantial part of it. Our results identify a volatility parameterization that performs reliably under NO_x-rich conditions and delineate the sensitivities that must be constrained before residual nanoparticle growth can be attributed to specific mechanisms.

Published by Copernicus Publications on behalf of the European Geosciences Union.

1 Introduction

Formation of atmospheric new aerosol particles via gas-to-particle conversion is a key source of cloud condensation nuclei (CCN) (Dunne et al., 2016; Gordon et al., 2017), but only if nascent particles grow fast enough to escape the scavenging-prone sub-15 nm size range (Kuang et al., 2009). Condensation of sulfuric acid (H_2SO_4) and low-volatility oxygenated organic molecules (OOMs) are believed to driver this initial growth in the urban and forest atmosphere (Mohr et al., 2019; Qiao et al., 2021; Stolzenburg et al., 2025). Closure between simulation and observed growth rates (GRs) has been reported in selected atmospheric environments, including the boreal forest in Hyytiälä, Finland (Mohr et al., 2019), and roadside locations in Leipzig, Germany (Brean et al., 2024). However, broader observations enabled by multi-instrument OOM detection show that closure often fails across regions and seasons, with models under- or over-predicting 3-15 nm particle growth, for example in urban Beijing (Qiao et al., 2021) and again in Hyytiälä under different seasonal conditions (Stolzenburg et al., 2025). Such discrepancies, reflecting both model uncertainties and unrepresented growth mechanisms, bias estimates of global CCN and aerosol–cloud radiative effects and degrade air-quality forecasts (Carslaw et al., 2013; Gordon et al., 2017; Kulmala, 2025).

The main challenge in accurately quantifying the contribution of OOMs to nanoparticle growth lies in the uncertainties associated with their concentration and volatility (Mohr et al., 2019; Tröstl et al., 2016). While uncertainties in concentration measurements of OOMs by Chemical Ionization Mass Spectrometer (CIMS) can be generally constrained to $\sim 50\,\%$, yielding growth-rate uncertainties below $\sim 60\,\%$ in typical urban or boreal forest environments, direct volatility measurements for individual OOMs remain extremely challenging owing to their very low vapor pressures and the lack of synthetic standards (Lopez-Hilfiker et al., 2016; Qiao et al., 2021; Sekimoto et al., 2017; Stolzenburg et al., 2025). As an alternative, typical volatility parameterizations may carry uncertainties of up to several orders of magnitude, potentially leading to errors by a factor of ~ 3–4 in simulated nanoparticle GRs (Donahue et al., 2011; Li et al., 2016; Mohr et al., 2019; Ren et al., 2022; Stolzenburg et al., 2018, 2025; Wang et al., 2020; Yang et al., 2023).

Given these large uncertainties in OOM volatility, it remains unclear whether coagulation and condensation alone can account for the observed growth of freshly formed nanoparticles, and how well current volatility parameterizations perform under different atmospheric regimes. Here, we present laminar flow reactor experiments that quantitatively resolve the respective contributions of particle-particle coagulation and OOM condensation to nanoparticle growth, thereby enabling a direct, controlled evaluation of widely used OOM volatility parameterizations against observed growth. We examine OOMs generated from α-pinene and toluene oxidation across a range of seed particle sizes (3–5 nm) and NO_x conditions, and then apply the best-performing, laboratory-validated parameterization to NPF events observed at Lake Tai, China, in summer 2023 to assess the extent to which coagulation and vapour condensation can explain the growth of ambient 3–15 nm nanoparticles.

2 Methods

2.1 Laminar flow reactor and experimental setup

A custom-designed laminar flow reactor was constructed to investigate the condensational growth of seed particles in the presence of OOMs, with three functional modules: seed-particle generation, OOM generation, and the main growth region (Fig. S1 in the Supplement; full geometric and operational details in Supplement, Sect. S1).

Self-charged polydisperse Ni-Cr seed nanoparticles were produced by resistive heating of a nichrome wire and classified to a monodisperse size distribution using a high-resolution half-mini differential mobility analyzer (half-mini-DMA) (Liu et al., 2020), yielding a dimensionless resolving power ($R = Z/\Delta Z$) of ~ 30 at a mobility diameter of 3.3 nm. The monodisperse outflow was split between a fast condensation particle counter (Fast CPC; Model 3650, Kanomax Inc., Japan) for online seed-number monitoring and the inlet of the laminar flow reactor.

OOMs were generated by hydroxyl radical (OH)-initiated oxidation of toluene or ozonolysis of α-pinene in a Potential Aerosol Mass (PAM) oxidation flow reactor (Aerodyne Research Inc.) operated at a residence time of ~ 52 s. For OH + toluene experiments, the PAM was run in the OFR254 mode, with OH generated in situ by 254 nm photolysis of O_3 in the presence of water vapor; for α-pinene experiments, the PAM operated as a dark ozonolysis reactor without UV. NO was added in selected experiments to produce controlled NO_x levels, and 2.5 sccm of 10 % CO was injected at the PAM outlet as an OH scavenger to terminate downstream oxidation. Relative humidity was maintained at 44 %–53 %; experimental conditions are summarized in Table S1 in the Supplement.

The ozonolysis of α-pinene experiments were performed under dark condition without UV irradiation, so elevated OH only concerns the toluene + OH experiments. In these experiments, the average OH concentration in the PAM reactor was about $2\text{–}6 \times 10^9$ molecules cm^{-3} resulting in OH exposure of $1.2\text{–}3.2 \times 10^{11}$ molecules cm^{-3} s, and much higher than typical ambient values in the Yangtze River Delta (0.8–2.4×10^7 molecules cm^{-3}; Wang et al., 2024). Such conditions favour $RO_2 + OH$ over autoxidation, which may shift the products from highly oxygenated molecules towards less oxygenated and multi-generation species (Peng et al., 2019; Wang et al., 2024). However, under the high-NO_x conditions of our experiments, $RO_2 + NO$ remains the dominant RO_2 pathway, as that in urban Beijing (Wang et al., 2024). Previ-

ous comparisons between flow-reactor, chamber and ambient products also show the same product families, with differences mainly in their relative abundances (Garmash et al., 2020; Cheng et al., 2021). The distribution of OOMs in our experiments may therefore differ from that in the ambient atmosphere, but the types of OOMs formed remain representative of ambient OOMs, which is the basis for our evaluation of the volatility parameterizations.

Seed nanoparticles and OOMs entered the growth region (200 cm long, 20 cm i.d.) through a coaxial inlet design (axial conical inlet for particles, annular inlet for OOMs) that promotes rapid radial mixing while preserving laminar flow ($Re < 200$). At a total flow of 21 L min^{-1}, the residence time was ~ 3 min. Nine axial sampling ports, distributed at 20 cm intervals starting 35 cm downstream of the OOM injection plane, enabled time-resolved measurements of particle size and number with a TSI® 1 nm SMPS (Model 3938E57), and of OOM concentrations with three online mass spectrometers (Vocus-PTR, iodide-CIMS, and nitrate-CIMS; Aerodyne Research Inc., USA and Tofwerk AG, Switzerland). A particle size magnifier (PSM; Model A10, Airmodus Inc., Finland) and a nano-SMPS (Model 3936, TSI Inc., USA) at the 180 s port verified the absence of new particle formation under condensation conditions.

2.2 Generation and quantification of citric acid and PEG-7 vapors

Citric acid (saturation vapor pressure estimated by group contribution methods; Moller et al., 2008; Nannoolal et al., 2004; and validated against FIGAERO-iodide-CIMS measurements; Ren et al., 2022; Ye et al., 2019) and PEG-7 (with a directly measured vapor pressure; Krieger et al., 2018) were generated by passing zero-air over heated reservoirs (45–80 °C for citric acid; 52–85 °C for PEG-7). Citric acid was quantified with the nitrate-CIMS and PEG-7 with the iodide-CIMS, using liquid-injection calibrations (calibration factors: 1.35×10^{12} cm^{-3} for citric acid and 9.44×10^{11} cm^{-3} for PEG-7; Fig. S2).

2.3 Measurement and quantification of OOMs

Gas-phase OOMs (defined as molecules containing at least one C, H, and O atom) were measured by three complementary mass spectrometers, all equipped with long time-of-flight analyzers (mass resolution 8000–9000 Th Th^{-1}). Each of the three ionization schemes carries a characteristic detection bias, and their combination does not amount to a complete coverage of the condensable vapour population. Efficient clustering with NO_3^- requires several hydrogen-bond-donating groups, so that the nitrate-CIMS underdetects less-oxygenated species and multifunctional carbonyls or esters that lack –OH and –OOH functionality. The iodide-CIMS detects polar and acidic species efficiently but discriminates against weakly binding, low-polarity compounds, a bias we quantify through the declustering-voltage scans described above (Fig. S3). The Vocus-PTR fragments multifunctional species, in particular peroxides and organic nitrates, biasing their quantification to the low end. The classes most likely to be underdetected are therefore ROOR′-type peroxides, weakly polar multifunctional carbonyls, and sulfur-containing organics. These biases do not act uniformly across the volatility range. Growth of sub-15 nm particles is controlled by species of sufficiently low volatility to overcome the Kelvin barrier, which are the highly oxygenated compounds to which the nitrate-CIMS is most sensitive, whereas undetected compounds are expected to be volatile ones.

The Vocus-PTR was calibrated using a multi-component gas-phase standard (Table S2), and sensitivities for non-calibrated OOMs were estimated from their proton-transfer reaction rate constants (Sekimoto et al., 2017) (Fig. S4). The iodide-CIMS followed the Lopez-Hilfiker et al. (2016) calibration scheme, with declustering-voltage scans converting iodide–OOM adduct stabilities (dV_{50}) into compound-specific sensitivities (Table S3 and Fig. S3). The nitrate-CIMS was calibrated assuming OOMs ionize at the H_2SO_4 collision limit (Tröstl et al., 2016; Yao et al., 2018), with mass-dependent transmission corrections (Heinritzi et al., 2016). Estimated systematic uncertainties are ±20 % (Vocus-PTR, calibrated species), ~ 60 % (iodide-CIMS, OOM mixtures), and ± 50 % (nitrate-CIMS).

For OOMs detected by multiple instruments, concentrations were assigned according to the oxygen number (n_O): nitrate-CIMS for $n_O \geq 6$; iodide-CIMS for $n_O \leq 3$ (vs. nitrate-CIMS) or $n_O \geq 4$ (vs. Vocus-PTR); Vocus-PTR for $n_O \leq 1$. For overlapping intermediate ranges ($n_O = 4$–5 between iodide and nitrate; $n_O = 2$–3 between iodide and Vocus-PTR), the higher of the two estimates was used (Figs. S5 and S6). Real-time axial concentration profiles of each OOM along the flow reactor were derived from regression of measured concentrations against residence time at the nine sampling ports (Fig. S7) and used as input to the growth model. See details in Sect. S2. Sulfur-containing OOMs were also detected in the ambient measurements, but because of their low abundance, they were not included in the growth simulations

2.4 Volatility parameterization and growth simulation

Saturation concentrations C^* of individual OOMs were estimated from their molecular formulas using published parameterizations; the Zhang et al. (2026) scheme is given by

$$\log_{10}C^*(300\,\mathrm{K}) = (25-n_C)b_C - (n_O-3n_N)b_O - 2\frac{(n_O-3n_N)n_C}{(n_C+n_O-3n_N)}b_{CO} - n_N b_N \quad (1)$$

$b_C = 0.493$, $b_O = 1.392$, $b_{CO} = -0.532$, and $b_N = 2.402$ from Zhang et al. (2026). C^* was corrected to ambient temperature using a vaporization enthalpy $\Delta H_{vap} = -5.7\log_{10}C^*(300\,\mathrm{K}) + 129\,\mathrm{kJ\,mol^{-1}}$ (Sect. S3).

The volatility parameterizations carry uncertainties that should be considered when interpreting the C^* values used here. They arise from (i) the assignment of a single C^* to each molecular formula, whereas isomers can differ substantially in vapour pressure; (ii) the limited range of compounds and conditions used to calibrate each scheme; (iii) the uncertainty of the reference data, since direct volatility measurements of gas-phase OOMs are scarce. When compared with the NCI open database, the Zhang et al. (2026) scheme performs comparably to the other schemes for CHO compounds and agrees more closely for CHON compounds. Nanoparticle growth was simulated following the Stolzenburg et al. (2022) monodisperse VBS framework, which solves the coupled mass-transfer equations for OOM condensation across volatility bins together with kinetically limited H_2SO_4 condensation. Particle-phase activity, Kelvin correction, and hard-sphere collision kernels are described in Sect. S4. H_2SO_4 was measured by the nitrate-CIMS (calibration factor 8.03×10^9 cm^{-3}).

3 Field measurements

A field campaign was conducted from 4 July to 20 September 2023 at the National Field Observation and Research Station for the Lake Ecosystem of Lake Tai (31°42′ N, 120°22′ E; ∼ 5 m above sea level), a suburban site in Jiangsu Province, China, influenced by both anthropogenic and biogenic emissions. PNSDs from 1.2 to 700 nm were measured in parallel by a TSI® 1 nm SMPS, a TSI® Long-SMPS, and an Airmodus® PSM at 1–4 min resolution. Twelve NPF events were observed, four of which were selected for detailed analysis based on moderate background condensation sinks and smooth growth behavior. Gas-phase OOMs at the site were measured using the same nitrate-CIMS, iodide-CIMS, and Vocus-PTR as in the laboratory, with sampling configurations detailed in Sect. S5.

4 Results and discussion

4.1 Condensation-driven growth of nanoparticles

A laminar flow reactor (Fig. S1a) was developed to investigate the growth of nanoparticles through particle-particle coagulation and condensation of organics. This laminar flow reactor sets the beginning of exposure upon the particle-vapor mixing and a residence time of 180 s at the 9th axial sampling point with a total flow rate of 21 L min^{-1}. Self-charged Ni-Cr oxide nanoparticles were generated by resistive heating of a nichrome wire, classified to a monodisperse diameter using a custom-made half-mini-DMA with peak number concentrations of $(1.5\text{–}2.0) \times 10^5$ cm^{-3} ($\mathrm{d}N/\mathrm{d}\log D_\mathrm{p}$, cm^{-3}), and then introduced into the laminar flow reactor (Liu et al., 2021) (Sect. S1 and Fig. S8). The evolution of number concentrations and mode diameters of charged Ni-Cr oxide nanoparticles was measured by a TSI® 1 nm SMPS at nine axial sampling points along the growth region. Owing to the limited resolving power of the 1 nm SMPS ($R = Z/\Delta Z \approx 7$ at 3.3 nm), the geometric standard deviations (GSDs) of measured particle number size distributions (PNSDs) ($\mathrm{GSD}_{1\,\mathrm{nmSMPS}} < 1.08$) were slightly larger than the true values obtained from the half-mini-DMA ($\mathrm{GSD}_{\mathrm{half-mini-DMA}} = 1.01$); the mode diameters, however, were unaffected (Fig. S8). No measurable increase in mode diameter was observed over the 180 s residence time (Fig. 1a), consistent with the < 0.1 nm increase predicted by inter-particle coagulation simulations (Cai et al., 2021). The simulation also predicts a coagulation-driven number loss rate of 0.01 % s^{-1}; subtracted from the observed number loss rate of 0.11 % s^{-1}, this yields a wall-loss rate of 0.10 % s^{-1} for 3.3 nm Ni-Cr oxide nanoparticles.

The monodisperse Ni-Cr oxide nanoparticles were then exposed to two condensable vapors with well-characterized volatilities in two separate sets of experiments: polyethylene glycol-7 (PEG-7), whose saturation vapor pressure has been experimentally measured (Krieger et al., 2018), and citric acid, whose saturation vapor pressure was estimated by group contribution methods (Moller et al., 2008; Nannoolal et al., 2004) and validated against FIGAERO-iodide-CIMS measurements (Ren et al., 2022; Ye et al., 2019). Gaseous citric acid concentrations in four experiments – including a reference experiment (Exp. 1) in which no citric acid was introduced (Fig. 1b) – were measured at the 180 s sampling port by a nitrate ion-based chemical ionization mass spectrometer (nitrate-CIMS); concentrations along the reactor axis (Fig. 1c) were inferred from the experimentally determined first-order wall-loss rate constant of citric acid (Fig. S9). Correspondingly, the mode diameter of the seed nanoparticles increased from 3.3 to 3.4, 3.6, and 3.8 nm under three increasing citric acid concentrations (Fig. 1d). Parallel experiments with PEG-7 (Exp. 5–8 in Fig. S10) produced comparable concentration-dependent growth.

We then simulated nanoparticle growth from the measured saturation vapor pressures and axial concentration profiles of citric acid or PEG-7 (Sect. S6 and Fig. S9). The simulation is advanced with a 1 s time step, and at each step the equilibrium vapour pressure of the condensing species is evaluated at the particle diameter reached in the preceding step, so that the curvature-affected equilibrium vapour pressure is tracked continuously as the particle grows. Figure 1e compares the measured GRs with simulated values across the concentration ranges examined. A strong correlation between measured and simulated GRs was observed, with data points generally scattered within a factor of 1.5 along the 1 : 1 line, confirming that our growth model accurately reproduces condensation-driven nanoparticle growth.

4.2 Evaluation of volatility parameterizations

Next, we investigated OOM-mixture-driven growth of monodisperse Ni-Cr oxide nanoparticles using OOMs gen-

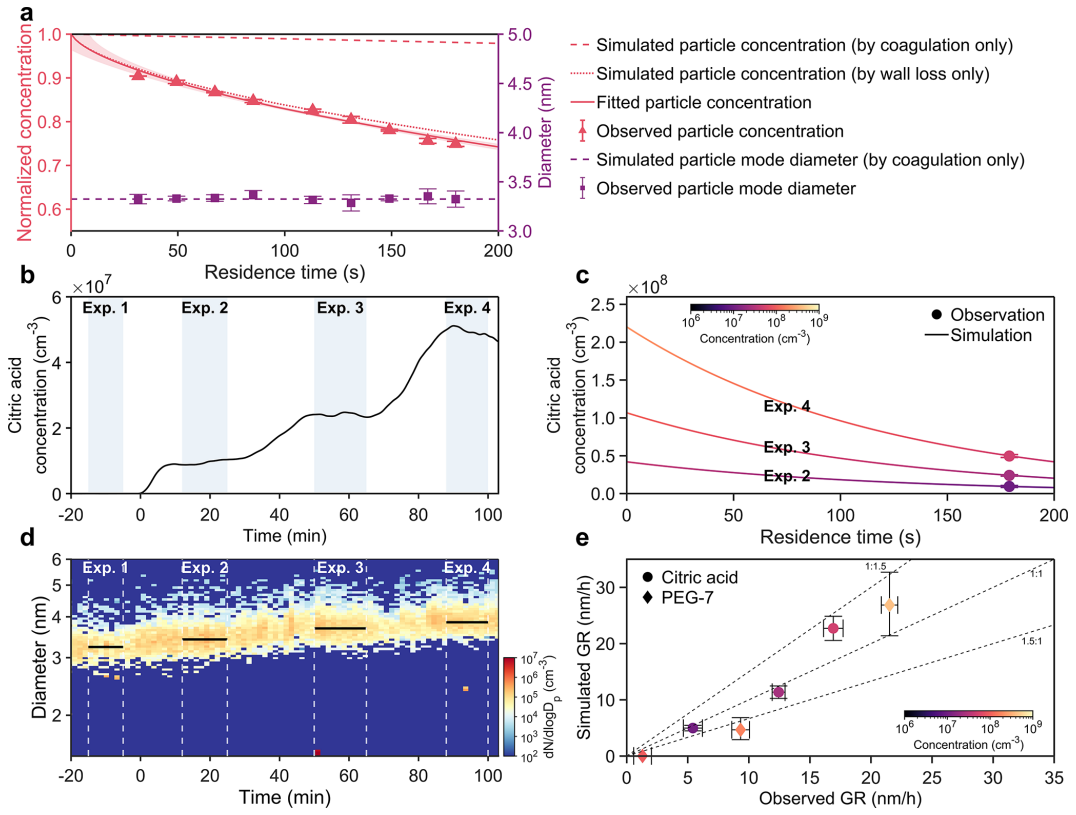


Figure 1. Coagulation- and condensation-driven growth of monodisperse Ni-Cr oxide nanoparticles in a laminar flow reactor. **(a)** Normalized number concentrations (red triangles) and mode diameters (purple squares) of Ni-Cr oxide nanoparticles at nine sampling points. The dashed purple line and dashed red line illustrate theoretical evolutions of the particle mode diameter and number, respectively, due to coagulation. The solid red line represents the observed decay of Ni-Cr oxide nanoparticle concentration, which, together with the red dashed line, gives the red dotted line indicating wall losses of Ni-Cr oxide nanoparticles. **(b)** Citric acid concentrations measured by nitrate-CIMS at a fixed residence time of 180 s in the laminar flow reactor; light blue shaded intervals denote Exp. 1–4, among which the citric acid exposure was zero in Exp. 1. **(c)** Observed citric acid concentrations at a residence time of 180 s for Exp. 2–4. Colored lines represent back-calculated concentrations of citric acid with incorporation of wall loss using the loss-rate coefficient of citric acid (refer to Fig. S9). **(d)** Particle number size distributions (PNSDs) of Ni-Cr oxide nanoparticles during Exp. 1–4. Vertical dashed white lines mark experimental boundaries, and horizontal black lines indicate the mean mode particle diameter in each experiment. **(e)** Comparison of experimentally measured particle GRs and simulated ones when exposing nanoparticles to citric acid or PEG-7. Circles and diamonds represent citric acid and PEG-7 experiments, respectively, under varying concentrations. The dashed lines depict 1 : 1, 1 : 1.5, and 1.5 : 1 reference ratios, and error bars for a datapoint indicate one standard deviation of the measurement mean.

erated from the oxidation of toluene or α-pinene under high and low NO_x in the laminar flow reactor (Table S1). As an illustrative example, 3.3 nm Ni-Cr oxide nanoparticles were exposed to OOMs from α-pinene ozonolysis under low-NO_x conditions; the OOM abundances were controlled by varying the α-pinene concentration. Four quasi-steady sampling periods (Exp. 9–12) captured successive growth stages (Fig. 2a, b). Note that the residual OOMs detected in Exp. 9 (Fig. 2a) before O_3 introduction did not produce measurable particle growth; the particle size measured at the 131 s sampling port in Exp. 9 was therefore used as the initial particle size (3.3 nm) at $t = 0$ s (Fig. 2c). In the other three experiments (Exp. 10–12), the mode diameter of the seed nanoparticles increased from 3.3 to 3.5, 3.7, and 3.9 nm (Fig. 2c), corresponding to GRs of 5.5, 11.0, and 16.5 nm h^{-1}, respectively.

Figure 2d presents a mass defect plot of all detected OOMs. Species were measured by three complementary instruments: a Vocus proton-transfer-reaction mass spectrometer (Vocus-PTR), an iodide-ion-based chemical ionization mass spectrometer (iodide-CIMS), and a nitrate-ion-based chemical ionization mass spectrometer (nitrate-CIMS), with many species detected by two or all three instruments. Concentrations of individual OOMs were quantified by instrument-specific calibrations (see Sect. 2.3). Note that identical molecular formulas across instruments do not necessarily correspond to identical structures, given the diversity of possible isomers.

For OOMs detected by both iodide-CIMS and nitrate-CIMS, the two estimates agreed within an order of magnitude only for species with oxygen number (n_O) = 4–5, while

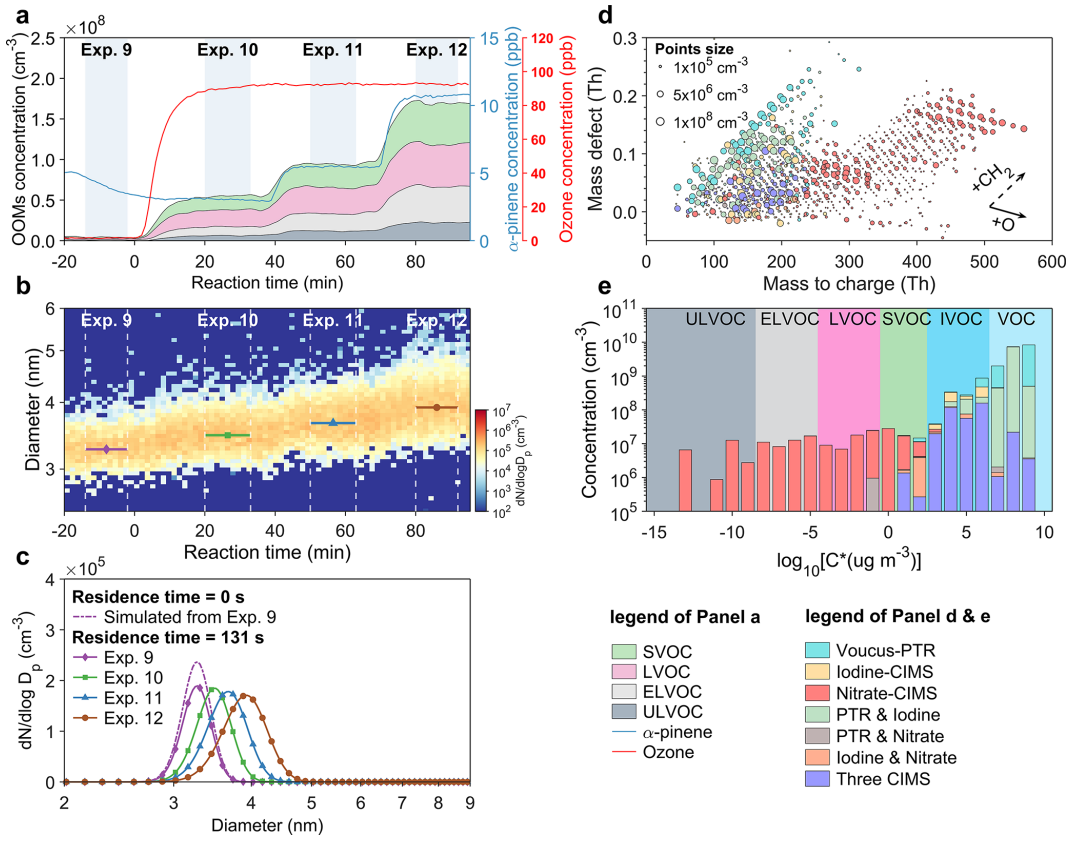


Figure 2. Particle growth driven by condensation of OOMs formed from α-pinene + O_3 under low NO_x conditions. **(a)** Profiles of gas-phase precursors and total concentrations of SVOC, LVOC, ELVOC, and ULVOC during four experiment periods (Exp. 9–12) as highlighted in shaded regions. **(b)** PNSDs of Ni-Cr oxide nanoparticles during Exp. 9–12. Vertical dashed white lines mark experimental boundaries, and horizontal-colored lines indicate the mean mode particle diameter in each experiment. **(c)** PNSDs in Exp. 9–12. The dashed line represents the simulated size distribution at a residence time of 0 s based on Exp. 9. The solid lines represent measured PNSDs at a residence time of 131 s for Exp. 9–12, illustrating particle growth resulting from condensation of varying concentrations of OOMs. **(d)** Mass defect plot for all assigned OOMs in Exp. 12. Marker size scales with OOMs' concentration. Marker color indicates which of the three CIMS (Vocus-PTR, iodide-CIMS, nitrate-CIMS) detected the OOMs, including overlaps, following the color scheme in the bottom right panel. **(e)** OOM concentration as a function of effective saturation concentration ($\log_{10}C^*$), grouped into volatility classes (ULVOC → VOC). Volatility estimates of OOMs are derived using the parameterization of Zhang et al. (2026). Bars show the concentrations of OOMs detected by at least one of three CIMS, following the color scheme in the bottom-right panel. Please refer to the main text for quantification rules.

diverging systematically at lower or higher oxygen numbers (Fig. S5). Because CIMS sensitivity depends strongly on the oxygen number (n_O) of OOMs (Riva et al., 2019), formulas with $n_O \leq 3$ were quantified by iodide-CIMS, those with $n_O \geq 6$ by nitrate-CIMS, and those with $n_O = 4$–5 were assigned the higher of the two estimates. For OOMs detected by both Vocus-PTR and iodide-CIMS, the two estimates showed larger discrepancies than for the iodide-CIMS / nitrate-CIMS pair (Fig. S6), reflecting fragmentation of multifunctional OOMs in Vocus-PTR (Li et al., 2022; Zhang et al., 2025). Following the same logic, formulas with $n_O = 0$ or 1 were quantified by Vocus-PTR, those with $n_O \geq 4$ by iodide-CIMS, and those with $n_O = 2$ or 3 were assigned the higher of the two estimates. For OOMs detected by both Vocus-PTR and nitrate-CIMS, the nitrate-CIMS estimate was used. For species detected by all three instruments, the iodide-CIMS / nitrate-CIMS rule was applied and the Vocus-PTR estimate was discarded. Importantly, the OOMs with the largest discrepancies ($n_O < 4$) are sufficiently volatile that they do not contribute to sub-15 nm particle growth owing to the Kelvin effect (Fig. S11); their impact on simulated GRs is therefore limited.

We then applied seven volatility parameterizations to the OOMs detected in Exp. 12 to calculate their saturation vapor concentrations, yielding seven Volatility Basis Set (VBS) representations spanning ultra-low-volatility, extremely low-volatility, low-volatility, semi-volatile, intermediate-volatility, and volatile organic compounds (ULVOC, ELVOC, LVOC, SVOC, IVOC, and VOC) (Figs. 2e and S12). Although all seven schemes spanned the full ULVOC-VOC range, they showed systematic offsets in their assigned $\log_{10}C^*$ values, leading to markedly different

volatility distributions. The Zhang et al. (2026) scheme is shifted most strongly toward higher volatility, assigning 91 % of OOMs to VOCs and 8 % to IVOCs, with only 0.67 % combined in ULVOC, ELVOC, and LVOC (Fig. 2a).

Table S4 summarizes the seven parameterizations including the reaction systems or chemicals from which they were derived, and their required molecular descriptors and intended applications. The seven schemes mainly differ in the volatility datasets upon which they were built. Six of them rest mainly on chamber-generated oxidation oxygenated products from biogenic precursors, which are dominated by CHO compounds. In contrast, the scheme of Zhang et al. (2026) was calibrated against the volatilities measured directly from ambient particulate OOMs at urban and suburban sites. These OOMs are formed in the presence of NO_x and include N-containing species, so that the scheme is constrained over a wider part of formula space whereas the other schemes sample only weakly. In a comparison with the scheme derived from the National Cancer Institute (NCI) open database, this scheme performed comparably to the other schemes for CHO compounds and better than others for CHON compounds. Therefore, it can be expected to more realistically describe the volatility of OOMs formed under high-NO_x conditions, consistent with its closer agreement with our laboratory growth experiments (Sect. 3.2).

We then compared the measured PNSDs for Exp. 12 with those simulated from the measured concentration profiles in the flow reactor (Fig. S12) and the parameterized volatilities (Fig. 2e) of individual OOMs. All seven simulated PNSDs overestimated the observed particle growth to varying degrees (Fig. 3a): the Zhang et al. (2026) parameterization showed the smallest overestimation, followed by Li et al. (2016), Mohr et al. (2019), and Dada et al. (2023). When nanoparticles were exposed to OOMs formed from α-pinene + O_3 under high-NO_x conditions (Exp. 13–16; Fig. S13), the Li et al. (2016), Mohr et al. (2019), and Dada et al. (2023) parameterizations exhibited substantially larger overestimations than under low-NO_x conditions (Fig. 3b), whereas the Zhang et al. (2026) parameterization continued to perform best. This is consistent with the better agreement between the Zhang et al. (2026) parameterization and CHON-compound volatilities tabulated in the National Cancer Institute (NCI) open database.

To assess the generality of these findings, we examined experiments spanning different seed nanoparticle diameters (3–5 nm) and OOM types from either toluene + OH or α-pinene + O_3 under low- or high-NO_x conditions (Exp. 9–56 in Table S1; Figs. 2a–d, S13–S15 for growth experiments and Figs. 2e, S16–S18 for volatility parameterizations). The simulated-to-measured GR ratios for all conditions are summarized in Fig. 3c. The Stolzenburg et al. (2025) and Qiao et al. (2021) schemes systematically overpredicted growth across a wide range of conditions. Notably, both schemes were developed from volatility frameworks largely constrained by biogenic volatile organic compounds (BVOC) oxidation chemistry: Stolzenburg et al. (2025) refined the formulation using BVOC autoxidation products, whereas Qiao et al. (2021) built on the revision by Mohr et al. (2019), which was derived from HOM measurements of α-pinene oxidation. By contrast, the Li et al. (2016), Mohr et al. (2019), Stolzenburg (2018), and Dada et al. (2023) schemes reproduced the measured GRs under low-NO_x conditions but overpredicted growth under high-NO_x conditions, particularly for OOMs from toluene + OH oxidation, which are more representative of urban atmospheres. Together, these results suggest that BVOC-derived volatility frameworks describe OOM-driven growth reasonably well in relatively clean, low-NO_x regimes (e.g., α-pinene + O_3 oxidation). They are less transferable to polluted, high-NO_x environments, where anthropogenic precursors and intensified NO_x pathways likely generate OOM populations with distinct functionality, volatility, and condensational behavior.

4.3 Ambient nanoparticle growth

We analyzed field NPF events at Lake Tai, China in summer 2023, focusing on gaseous molecular compositions and PNSDs (see Sect. 2.5). High-resolution mass spectrometry measurements from Vocus-PTR, iodide-CIMS, and nitrate-CIMS revealed a wide molecular diversity of ambient gaseous OOMs, with each instrument capturing OOMs of different volatility and oxidation states, as illustrated by an example on 30 July 2023 (Fig. 4a, b). The volatility classification of ambient OOMs (Fig. 4b), based on estimated saturation concentrations (C^*) using the Zhang et al. (2026) scheme, indicates that a substantial fraction (0.39 %) of detected species fell into the ELVOC and LVOC classes.

Figure 4c presents a comparison of observed and simulated growth trajectories of newly formed nanoparticles following their formation on 30 July 2023. The growth of 3 nm nanoparticles was simulated as the sum of particle coagulation, H_2SO_4 condensation, and OOM condensation using OOMs volatilities from seven parameterization schemes. Among all schemes, Zhang et al. (2026) was the only one that underpredicted particle growth, whereas the others overpredicted growth to varying degrees. Together with our laboratory results, this pattern suggests that commonly used parameterizations assign OOMs volatilities that are too low, thereby overstating their condensational contribution to early nanoparticle growth. For example, the calculated GRs were larger than the measured ones in Hyytiälä, Finland, which was previously explained by evaporation of particulate matter but could stem from the parametrization itself (Stolzenburg et al., 2025). Figure 4d focuses on the comparison between the observed nanoparticle mode diameter evolution and the Zhang et al. (2026) scheme's prediction. Notably, the simulated mode diameters remained below the observed values and explained only 53 % of the 3–15 nm nanoparticle growth rate. An uncertainty envelope (−50 %/+50 %) was applied to OOM concentrations, yielding an uncertainty of

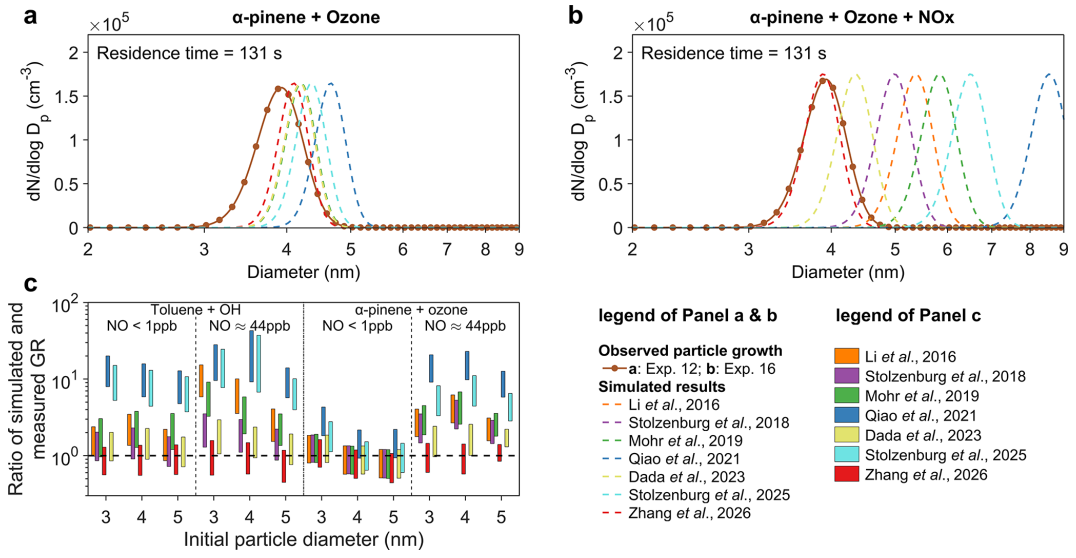


Figure 3. Comparison of observed and simulated growth of Ni-Cr oxide nanoparticles when exposed to OOMs. **(a)** Comparison of observed PNSDs (solid line) after exposing Ni-Cr oxide nanoparticles to OOMs formed from α-pinene $+ O_3$ oxidation under low NO_x conditions (Exp. 12), with simulated ones (dashed lines) using seven VBSs. **(b)** Comparison of observed PNSD (solid line) after exposing Ni-Cr oxide nanoparticles to OOMs formed from α-pinene $+ O_3$ oxidation under high NO_x conditions (Exp. 16), with simulated ones (dashed lines) using seven VBS schemes. **(c)** Ratios of simulated to measured GRs as a function of initial mode diameter under four OOM source scenarios: toluene + OH or α-pinene $+ O_3$ with low (NO $<$ 1 ppb) or high (NO $\approx$ 44 ppb) NO_x conditions. Colors and symbols indicate different GR simulation methods. The upper and lower bounds of the columns represent the simulation uncertainties associated with a +50 %/−50 % error in OOMs' concentrations. The dashed line represents the 1 : 1 reference.

approximately −45 % to +50 % for the condensation-driven growth. Even at the upper bound of this uncertainty range, the simulated 3–15 nm growth rate still left a residual ∼ 14 % gap relative to the observations. Beyond this single event, Fig. 4e presents the campaign-average behaviour across four NPF events (see Fig. S19 for details). The simulations systematically underestimated nanoparticle growth, particularly in the sub-15 nm size range, leaving a gap that the present framework does not explain. Several explanations for this gap are possible and not mutually exclusive: growth processes that the framework does not represent, condensable vapours that our instrumentation does not detect, and uncertainties in the measurements and in the growth model itself.

Among the processes that are not represented in the growth model, heterogeneous chemistry at nanoparticle surfaces is one plausible candidate: by converting relatively volatile gases into lower-volatility products that overcome the Kelvin barrier, it can drive growth even from highly volatile vapours (Wang et al., 2010). A box-model estimate that incorporates heterogeneous reactions of isoprene-derived epoxydiols (IEPOX)/methacrylic acid epoxide (IMAE), nitrogen oxides, and glyoxal/methylglyoxal substantially reduced this gap and brought the simulations toward the measurements (Fig. S20), indicating that gas–particle heterogeneous chemistry could be one potentially important yet currently unparameterized candidate contributor that merits dedicated investigation (see Sects. S7 and S8 for details).

On the other hand, several sources of uncertainty besides unrepresented mechanisms could contribute to the gap. First, the detection of condensable vapours is not necessarily complete: although three complementary mass spectrometers were deployed, it is likely that no combination of ionization schemes captures the entire condensable vapour population. In addition, species with low ionization efficiency towards NO_3^-, I^- and H_3O^+, thermally labile or strongly wall-adsorbing compounds, and condensable species falling outside our OOM definition would be missed. Second, the observed size distributions and growth rates also carry a potential uncertainty. Below 15 nm, this comes from low particle counts, the size-dependent efficiency of the 1 nm SMPS and PSM, and charging corrections. The method used to retrieve the growth rate adds further uncertainty (Cai et al., 2021). Third, the growth model is simplified. It assumes that particles are spherical and internally well mixed, with unit activity coefficients, and it neglects particle-phase reactions (such as oligomerization and chemical aging) and possible viscosity limitations to diffusion in freshly formed particles.

These results can be placed alongside recent attempts at growth closure. In boreal Hyytiälä, simulated GRs based on HOM condensation have been reported both to agree with observations (Mohr et al., 2019) and, in a more comprehensive analysis, to exceed them (Stolzenburg et al., 2025), the latter being attributed to evaporation of particulate organics; our laboratory evaluation suggests that at least part of such

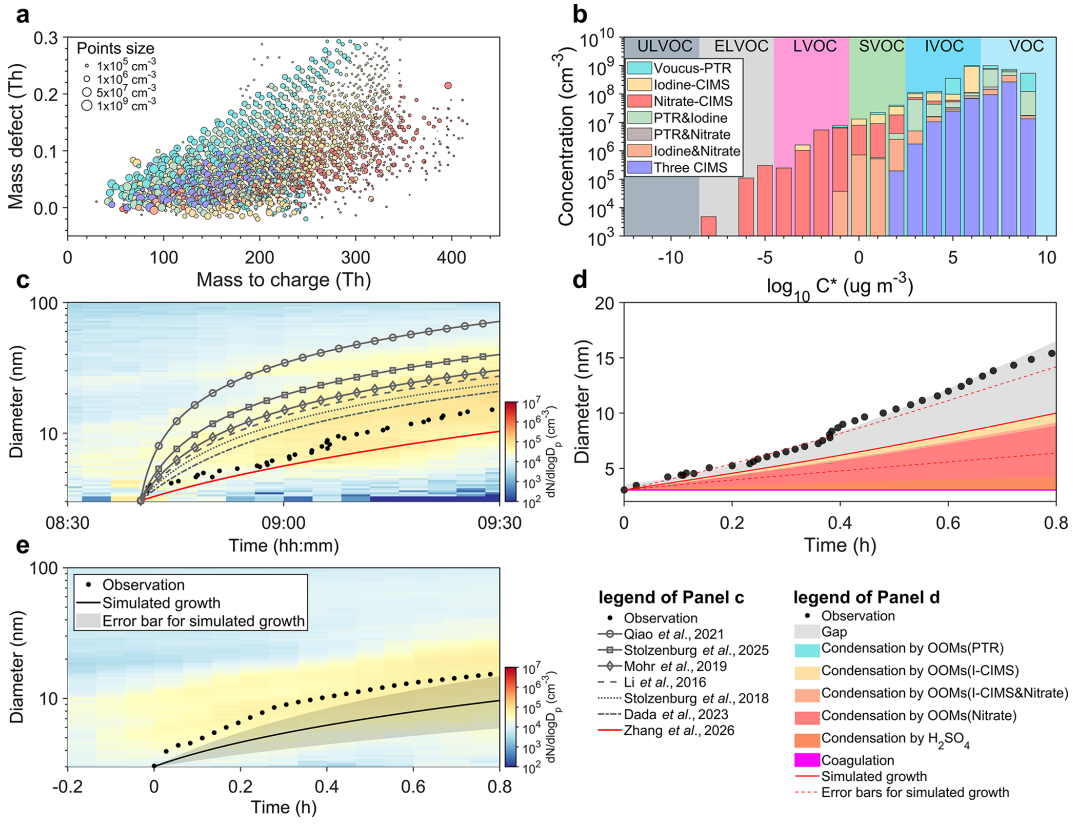


Figure 4. Characterization of ambient OOMs and their contribution to nanoparticle growth. **(a)** Mass defect plot of ambient OOMs detected at Lake Tai on 30 July 2023, using three CIMS; Marker color follows the legend in panel **(b)**, Marker size denotes the relative ion signal intensity. **(b)** Volatility distribution of ambient OOMs classified into ULVOC, ELVOC, LVOC, SVOC, IVOC, and VOC, based on estimated saturation concentrations. Bars show the concentrations of OOMs detected by at least one of the three CIMS. Please refer to the main text for quantification rules. **(c)** Evolution of nanoparticle mode diameter during an ambient NPF event in Lake Tai on 30 July 2023, overlaid on the PNSDs ($dN/d\log D_p$, cm^{-3}). Black dots represent the observed particle mode diameter. Modeled growth curves based on different volatility parameterization methods (Qiao et al., 2021; Mohr et al., 2019; Li et al., 2016; Stolzenburg et al., 2018, 2025; Dada et al., 2023; Zhang et al., 2026) are shown for comparison. **(d)** Decomposition of the observed ambient nanoparticle growth into contributions from OOM condensation, H_2SO_4 condensation, and coagulation of nanoparticles for a NPF event in Lake Tai on 30 July 2023. Black circles denote the observed mode diameter. The colored stacked areas show growth driven by coagulation of nanoparticles, condensation of H_2SO_4, and condensation of OOMs, respectively. The solid red line represents the simulated particle mode diameter. The grey shaded area ("Gap") indicates the unexplained growth not captured by these processes. The dashed red line marks the higher and lower uncertainty bounds of the simulated particle mode diameter from uncertainties in OOMs' concentrations. **(e)** Average PNSDs of four NPF events during the field campaign, with the particle mode diameter of 3 nm in all events serving as the starting point. Black dots represent the observed particle mode diameter. The black line gives the simulated growth based on particles coagulation and H_2SO_4 and OOMs condensation using the laboratory-validated volatility parameterization (Zhang et al., 2026), and black shadow denotes the uncertainty of the simulated diameter propagated from uncertainties in OOMs' concentrations.

an overprediction may originate in the volatility parameterization itself rather than in particle-phase evaporation. In urban Beijing, OOM condensation was found insufficient to close the observed growth of sub-10 nm particles (Qiao et al., 2021), whereas at a roadside site in Leipzig traffic-related vapours were sufficient to explain rapid growth (Brean et al., 2024). The sign of the closure error therefore appears to depend on the chemical regime at least as much as on the completeness of the measurement suite, consistent with the condition-dependent parameterization performance reported here.

5 Conclusions and outlook

This study examined whether condensation of H_2SO_4 and OOMs alone can account for the rapid growth of freshly nucleated nanoparticles. Using a laminar flow reactor that cleanly separates particle–particle coagulation from OOM condensation, we benchmarked seven widely used volatility parameterizations directly against observed growth. Across diverse OOM precursors (α-pinene and toluene), seed nanoparticle sizes (3–5 nm), and NO_x regimes, six of the seven overestimated nanoparticle growth-most severely un-

der the high-NO_x conditions typical of polluted urban airwhereas only a parameterization constrained by ambient organic-aerosol volatility (i.e., Zhang et al., 2026) reproduced our observations.

The overestimation arises because most existing parameterizations were derived from, or tuned to, biogenic, low-NO_x oxidation systems dominated by CHO compounds, and they tend to assign lower volatilities to the OOM populations generated under high-NO_x, anthropogenically influenced conditions. Such conditions favour nitrogen-containing products (e.g., organonitrates) and fragmentation pathways that shift the volatility distribution toward higher volatility, so that schemes calibrated on biogenic reaction systems overstate the condensation flux of organics. This interpretation is supported by the fact that the Zhang et al. (2026) parameterization, which is constrained by directly measured volatilities of ambient urban and suburban particulate OOMs, alone reproduces our observations. The fundamental insight is therefore not that any individual parameterization is inherently deficient, but that the volatility-composition relationship is sensitive to the chemical regime in which it is calibrated, particularly the prevailing NO_x level.

Whether the underprediction we observe at Lake Tai extends to other environments cannot be settled by a single campaign, and the performance of any volatility parameterization is expected to be regime-dependent. Our laboratory results nonetheless argue against a fixed low bias in the Zhang et al. (2026) scheme: under low-NO_x α-pinene $+ O_3$ conditions, it slightly overpredicted rather than underpredicted growth (Fig. 3a and c), so a systematic underprediction in a clean, BVOC-dominated environment such as Hyytiälä is not anticipated. Conversely, the scheme was derived from ambient particulate OOMs collected in a polluted region of eastern China and is best supported for NO_x-rich, mixed anthropogenic–biogenic conditions; its extrapolation to pristine biogenic or marine environments remains to be tested. The residual growth at Lake Tai is therefore more plausibly a property of the site (i.e., elevated NO_x, abundant anthropogenic precursors and reactive gas–particle chemistry) than a generic feature of the parameterization.

These caveats notwithstanding, the results caution against applying volatility frameworks calibrated largely on biogenic, clean-environment chemistry to polluted, high-NO_x atmospheres, where such frameworks may overstate the organic contribution to early growth and thereby bias estimates of CCN abundance and aerosol–cloud radiative forcing. Establishing a transferable, mechanistically complete description of nanoparticle growth will require extending these co-evaluated laboratory and field analyses to diverse polluted atmospheres, alongside direct volatility measurements and explicit kinetic treatment of particle-phase heterogeneous reactions.

Data availability. The data used to support the conclusions in this study are available at a public data repository of Zenodo via https://doi.org/10.5281/zenodo.23737227 (Li, 2026). Additional data related to this paper can be requested from the corresponding authors (lei_yao@fudan.edu.cn; lin_wang@fudan.edu.cn).

Supplement. The supplement related to this article is available online at https://doi.org/10.5194/acp-26-15721-2026-supplement.

Author contributions. LW conceived and led the study; CL and LW developed the methodology; CL, FZ, YYL, and YLL performed the laboratory experiments; CL, GY, SY, and YL performed the field measurements; CL and Z-XC analyzed the field data; CL, RC, Z-XC, and JA performed the simulations; CL and LW wrote the manuscript draft; all coauthors reviewed and edited the manuscript.

Competing interests. The contact author has declared that none of the authors has any competing interests.

Disclaimer. Publisher's note: Copernicus Publications remains neutral with regard to jurisdictional claims made in the text, published maps, institutional affiliations, or any other geographical representation in this paper. The authors bear the ultimate responsibility for providing appropriate place names. Views expressed in the text are those of the authors and do not necessarily reflect the views of the publisher.

Acknowledgements. The authors gratefully acknowledge the National Field Observation and Research Station for the Lake Ecosystem of Lake Tai for providing access to the observation site and supporting infrastructure during the 2023 summer field campaign.

Financial support. This research has been supported by the Ministry of Ecology and Environment, The People's Republic of China (Jing-Jin-Ji Regional Integrated Environmental Improvement-National Science and Technology Major Project (grant no. 2026ZD1209900)) and the National Natural Science Foundation of China (grant nos. 22127811 and 21925601).

Review statement. This paper was edited by James Allan and reviewed by two anonymous referees.

References

Brean, J., Rowell, A., Beddows, D. C. S., Weinhold, K., Mettke, P., Merkel, M., Tuch, T., Rissanen, M., Maso, M. D., Kumar, A., Barua, S., Iyer, S., Karppinen, A., Wiedensohler, A., Shi, Z., and Harrison, R. M.: Road Traffic Emissions Lead to Much Enhanced New Particle Formation through In-

creased Growth Rates, Environ. Sci. Technol., 58, 10664–10674, https://doi.org/10.1021/acs.est.3c10526, 2024.

Cai, R., Li, C., He, X.-C., Deng, C., Lu, Y., Yin, R., Yan, C., Wang, L., Jiang, J., Kulmala, M., and Kangasluoma, J.: Impacts of coagulation on the appearance time method for new particle growth rate evaluation and their corrections, Atmos. Chem. Phys., 21, 2287–2304, https://doi.org/10.5194/acp-21-2287-2021, 2021.

Carslaw, K. S., Lee, L. A., Reddington, C. L., Pringle, K. J., Rap, A., Forster, P. M., Mann, G. W., Spracklen, D. V., Woodhouse, M. T., Regayre, L. A., and Pierce, J. R.: Large contribution of natural aerosols to uncertainty in indirect forcing, Nature, 503, 67–71, https://doi.org/10.1038/nature12674, 2013.

Cheng, X., Chen, Q., Jie Li, Y., Zheng, Y., Liao, K., and Huang, G.: Highly oxygenated organic molecules produced by the oxidation of benzene and toluene in a wide range of OH exposure and NO_x conditions, Atmos. Chem. Phys., 21, 12005–12019, https://doi.org/10.5194/acp-21-12005-2021, 2021.

Dada, L., Stolzenburg, D., Simon, M., Fischer, L., Heinritzi, M., Wang, M., Xiao, M., Vogel, A. L., Ahonen, L., Amorim, A., Baalbaki, R., Baccarini, A., Baltensperger, U., Bianchi, F., Daellenbach, K. R., DeVivo, J., Dias, A., Dommen, J., Duplissy, J., Finkenzeller, H., Hansel, A., He, X.-C., Hofbauer, V., Hoyle, C. R., Kangasluoma, J., Kim, C., Kürten, A., Kvashnin, A., Mauldin, R., Makhmutov, V., Marten, R., Mentler, B., Nie, W., Petäjä, T., Quéléver, L. L. J., Saathoff, H., Tauber, C., Tomé, A., Molteni, U., Volkamer, R., Wagner, R., Wagner, A. C., Wimmer, D., Winkler, P. M., Yan, C., Zha, Q., Rissanen, M., Gordon, H., Curtius, J., Worsnop, D. R., Lehtipalo, K., Donahue, N. M., Kirkby, J., El Haddad, I., and Kulmala, M.: Role of sesquiterpenes in biogenic new particle formation, Sci. Adv., 9, eadi5297, https://doi.org/10.1126/sciadv.adi5297, 2023.

Donahue, N. M., Epstein, S. A., Pandis, S. N., and Robinson, A. L.: A two-dimensional volatility basis set: 1. organic-aerosol mixing thermodynamics, Atmos. Chem. Phys., 11, 3303–3318, https://doi.org/10.5194/acp-11-3303-2011, 2011.

Dunne, E. M., Gordon, H., Kürten, A., Almeida, J., Duplissy, J., Williamson, C., Ortega, I. K., Pringle, K. J., Adamov, A., Baltensperger, U., Barmet, P., Benduhn, F., Bianchi, F., Breitenlechner, M., Clarke, A., Curtius, J., Dommen, J., Donahue, N. M., Ehrhart, S., Flagan, R. C., Franchin, A., Guida, R., Hakala, J., Hansel, A., Heinritzi, M., Jokinen, T., Kangasluoma, J., Kirkby, J., Kulmala, M., Kupc, A., Lawler, M. J., Lehtipalo, K., Makhmutov, V., Mann, G., Mathot, S., Merikanto, J., Miettinen, P., Nenes, A., Onnela, A., Rap, A., Reddington, C. L. S., Riccobono, F., Richards, N. A. D., Rissanen, M. P., Rondo, L., Sarnela, N., Schobesberger, S., Sengupta, K., Simon, M., Sipilä, M., Smith, J. N., Stozkhov, Y., Tomé, A., Tröstl, J., Wagner, P. E., Wimmer, D., Winkler, P. M., Worsnop, D. R., and Carslaw, K. S.: Global atmospheric particle formation from CERN CLOUD measurements, Science, 354, 1119–1124, https://doi.org/10.1126/science.aaf2649, 2016.

Garmash, O., Rissanen, M. P., Pullinen, I., Schmitt, S., Kausiala, O., Tillmann, R., Zhao, D., Percival, C., Bannan, T. J., Priestley, M., Hallquist, Å. M., Kleist, E., Kiendler-Scharr, A., Hallquist, M., Berndt, T., McFiggans, G., Wildt, J., Mentel, T. F., and Ehn, M.: Multi-generation OH oxidation as a source for highly oxygenated organic molecules from aromatics, Atmos. Chem. Phys., 20, 515–537, https://doi.org/10.5194/acp-20-515-2020, 2020.

Gordon, H., Kirkby, J., Baltensperger, U., Bianchi, F., Breitenlechner, M., Curtius, J., Dias, A., Dommen, J., Donahue, N. M., Dunne, E. M., Duplissy, J., Ehrhart, S., Flagan, R. C., Frege, C., Fuchs, C., Hansel, A., Hoyle, C. R., Kulmala, M., Kürten, A., Lehtipalo, K., Makhmutov, V., Molteni, U., Rissanen, M. P., Stozkhov, Y., Tröstl, J., Tsagkogeorgas, G., Wagner, R., Williamson, C., Wimmer, D., Winkler, P. M., Yan, C., and Carslaw, K. S.: Causes and importance of new particle formation in the present-day and preindustrial atmospheres, J. Geophys. Res.-Atmos., 122, 8739–8760, https://doi.org/10.1002/2017jd026844, 2017.

Heinritzi, M., Simon, M., Steiner, G., Wagner, A. C., Kürten, A., Hansel, A., and Curtius, J.: Characterization of the mass-dependent transmission efficiency of a CIMS, Atmos. Meas. Tech., 9, 1449–1460, https://doi.org/10.5194/amt-9-1449-2016, 2016.

Krieger, U. K., Siegrist, F., Marcolli, C., Emanuelsson, E. U., Gøbel, F. M., Bilde, M., Marsh, A., Reid, J. P., Huisman, A. J., Riipinen, I., Hyttinen, N., Myllys, N., Kurtén, T., Bannan, T., Percival, C. J., and Topping, D.: A reference data set for validating vapor pressure measurement techniques: homologous series of polyethylene glycols, Atmos. Meas. Tech., 11, 49–63, https://doi.org/10.5194/amt-11-49-2018, 2018.

Kuang, C., McMurry, P. H., and McCormick, A. V.: Determination of cloud condensation nuclei production from measured new particle formation events, Geophys. Res. Lett., 36, https://doi.org/10.1029/2009gl037584, 2009.

Kulmala, M.: Importance of New Particle Formation for Climate and Air Quality, ACS EST Air, 2, 710–712, https://doi.org/10.1021/acsestair.5c00095, 2025.

Li, C.: Organic condensation derived from different volatility parameterizations and its implications for ambient nanoparticle growth, Zenodo [data set], https://doi.org/10.5281/zenodo.23737227, 2026.

Li, H., Almeida, T. G., Luo, Y., Zhao, J., Palm, B. B., Daub, C. D., Huang, W., Mohr, C., Krechmer, J. E., Kurtén, T., and Ehn, M.: Fragmentation inside proton-transfer-reaction-based mass spectrometers limits the detection of ROOR and ROOH peroxides, Atmos. Meas. Tech., 15, 1811–1827, https://doi.org/10.5194/amt-15-1811-2022, 2022.

Li, Y., Pöschl, U., and Shiraiwa, M.: Molecular corridors and parameterizations of volatility in the chemical evolution of organic aerosols, Atmos. Chem. Phys., 16, 3327–3344, https://doi.org/10.5194/acp-16-3327-2016, 2016.

Liu, Y., Attoui, M., Yang, K., Chen, J., Li, Q., and Wang, L.: Size-resolved chemical composition analysis of ions produced by a commercial soft X-ray aerosol neutralizer, J. Aerosol Sci., 147, 105586, https://doi.org/10.1016/j.jaerosci.2020.105586, 2020.

Liu, Y., Attoui, M., Li, Y., Chen, J., Li, Q., and Wang, L.: Characterization of a Kanomax® fast condensation particle counter in the sub-10 nm range, J. Aerosol Sci., 155, 105772, https://doi.org/10.1016/j.jaerosci.2021.105772, 2021.

Lopez-Hilfiker, F. D., Iyer, S., Mohr, C., Lee, B. H., D'Ambro, E. L., Kurtén, T., and Thornton, J. A.: Constraining the sensitivity of iodide adduct chemical ionization mass spectrometry to multifunctional organic molecules using the collision limit and thermodynamic stability of iodide ion adducts, Atmos. Meas. Tech., 9, 1505–1512, https://doi.org/10.5194/amt-9-1505-2016, 2016.

Mohr, C., Thornton, J. A., Heitto, A., Lopez-Hilfiker, F. D., Lutz, A., Riipinen, I., Hong, J., Donahue, N. M., Hallquist, M., Petäjä, T., Kulmala, M., and Yli-Juuti, T.: Molecular identification of organic vapors driving atmospheric nanoparticle growth, Nat. Commun., 10, 4442, https://doi.org/10.1038/s41467-019-12473-2, 2019.

Moller, B., Rarey, J., and Ramjugernath, D.: Estimation of the vapour pressure of non-electrolyte organic compounds via group contributions and group interactions, J. Mol. Liq., 143, 52–63, https://doi.org/10.1016/j.molliq.2008.04.020, 2008.

Nannoolal, Y., Rarey, J., Ramjugernath, D., and Cordes, W.: Estimation of pure component properties Part 1. Estimation of the normal boiling point of non-electrolyte organic compounds via group contributions and group interactions, Fluid Phase Equilibria, 226, 45–63, https://doi.org/10.1016/j.fluid.2004.09.001, 2004.

Peng, Z., Lee-Taylor, J., Orlando, J. J., Tyndall, G. S., and Jimenez, J. L.: Organic peroxy radical chemistry in oxidation flow reactors and environmental chambers and their atmospheric relevance, Atmos. Chem. Phys., 19, 813–834, https://doi.org/10.5194/acp-19-813-2019, 2019.

Qiao, X., Yan, C., Li, X., Guo, Y., Yin, R., Deng, C., Li, C., Nie, W., Wang, M., Cai, R., Huang, D., Wang, Z., Yao, L., Worsnop, D. R., Bianchi, F., Liu, Y., Donahue, N. M., Kulmala, M., and Jiang, J.: Contribution of Atmospheric Oxygenated Organic Compounds to Particle Growth in an Urban Environment, Environ. Sci. Technol., 55, 13646–13656, https://doi.org/10.1021/acs.est.1c02095, 2021.

Ren, S., Yao, L., Wang, Y., Yang, G., Liu, Y., Li, Y., Lu, Y., Wang, L., and Wang, L.: Volatility parameterization of ambient organic aerosols at a rural site of the North China Plain, Atmos. Chem. Phys., 22, 9283–9297, https://doi.org/10.5194/acp-22-9283-2022, 2022.

Riva, M., Rantala, P., Krechmer, J. E., Peräkylä, O., Zhang, Y., Heikkinen, L., Garmash, O., Yan, C., Kulmala, M., Worsnop, D., and Ehn, M.: Evaluating the performance of five different chemical ionization techniques for detecting gaseous oxygenated organic species, Atmos. Meas. Tech., 12, 2403–2421, https://doi.org/10.5194/amt-12-2403-2019, 2019.

Sekimoto, K., Li, S.-M., Yuan, B., Koss, A., Coggon, M., Warneke, C., and Gouw, J. de: Calculation of the sensitivity of proton-transfer-reaction mass spectrometry (PTR-MS) for organic trace gases using molecular properties, Int. J. Mass Spectrom., 421, 71–94, https://doi.org/10.1016/j.ijms.2017.04.006, 2017.

Stolzenburg, D., Fischer, L., Vogel, A. L., Heinritzi, M., Schervish, M., Simon, M., Wagner, A. C., Dada, L., Ahonen, L. R., Amorim, A., Baccarini, A., Bauer, P. S., Baumgartner, B., Bergen, A., Bianchi, F., Breitenlechner, M., Brilke, S., Mazon, S. B., Chen, D., Dias, A., Draper, D. C., Duplissy, J., Haddad, I. E., Finkenzeller, H., Frege, C., Fuchs, C., Garmash, O., Gordon, H., He, X., Helm, J., Hofbauer, V., Hoyle, C. R., Kim, C., Kirkby, J., Kontkanen, J., Kürten, A., Lampilahti, J., Lawler, M., Lehtipalo, K., Leiminger, M., Mai, H., Mathot, S., Mentler, B., Molteni, U., Nie, W., Nieminen, T., Nowak, J. B., Ojdanic, A., Onnela, A., Passananti, M., Petäjä, T., Quéléver, L. L. J., Rissanen, M. P., Sarnela, N., Schallhart, S., Tauber, C., Tomé, A., Wagner, R., Wang, M., Weitz, L., Wimmer, D., Xiao, M., Yan, C., Ye, P., Zha, Q., Baltensperger, U., Curtius, J., Dommen, J., Flagan, R. C., Kulmala, M., Smith, J. N., Worsnop, D. R., Hansel, A., Donahue, N. M., and Winkler, P. M.: Rapid growth of organic aerosol nanoparticles over a wide tropospheric temperature range, P. Natl. Acad. Sci. USA, 115, 9122–9127, https://doi.org/10.1073/pnas.1807604115, 2018.

Stolzenburg, D., Wang, M., Schervish, M., and Donahue, N. M.: Tutorial: Dynamic organic growth modeling with a volatility basis set, J. Aerosol Sci., 166, 106063, https://doi.org/10.1016/j.jaerosci.2022.106063, 2022.

Stolzenburg, D., Sarnela, N., Bianchi, F., Cai, J., Cai, R., Cheng, Y., Dada, L., Donahue, N. M., Grothe, H., Holm, S., Kerminen, V.-M., Lehtipalo, K., Petäjä, T., Sulo, J., Winkler, P. M., Yan, C., Kangasluoma, J., and Kulmala, M.: Incomplete mass closure in atmospheric nanoparticle growth, npj Clim. Atmos. Sci., 8, 75, https://doi.org/10.1038/s41612-025-00893-5, 2025.

Tröstl, J., Chuang, W. K., Gordon, H., Heinritzi, M., Yan, C., Molteni, U., Ahlm, L., Frege, C., Bianchi, F., Wagner, R., Simon, M., Lehtipalo, K., Williamson, C., Craven, J. S., Duplissy, J., Adamov, A., Almeida, J., Bernhammer, A.-K., Breitenlechner, M., Brilke, S., Dias, A., Ehrhart, S., Flagan, R. C., Franchin, A., Fuchs, C., Guida, R., Gysel, M., Hansel, A., Hoyle, C. R., Jokinen, T., Junninen, H., Kangasluoma, J., Keskinen, H., Kim, J., Krapf, M., Kürten, A., Laaksonen, A., Lawler, M., Leiminger, M., Mathot, S., Möhler, O., Nieminen, T., Onnela, A., Petäjä, T., Piel, F. M., Miettinen, P., Rissanen, M. P., Rondo, L., Sarnela, N., Schobesberger, S., Sengupta, K., Sipilä, M., Smith, J. N., Steiner, G., Tomè, A., Virtanen, A., Wagner, A. C., Weingartner, E., Wimmer, D., Winkler, P. M., Ye, P., Carslaw, K. S., Curtius, J., Dommen, J., Kirkby, J., Kulmala, M., Riipinen, I., Worsnop, D. R., Donahue, N. M., and Baltensperger, U.: The role of low-volatility organic compounds in initial particle growth in the atmosphere, Nature, 533, 527–531, https://doi.org/10.1038/nature18271, 2016.

Wang, L., Khalizov, A. F., Zheng, J., Xu, W., Ma, Y., Lal, V., and Zhang, R.: Atmospheric nanoparticles formed from heterogeneous reactions of organics, Nat. Geosci., 3, 238–242, https://doi.org/10.1038/ngeo778, 2010.

Wang, M., Chen, D., Xiao, M., Ye, Q., Stolzenburg, D., Hofbauer, V., Ye, P., Vogel, A. L., Mauldin, R. L., Amorim, A., Baccarini, A., Baumgartner, B., Brilke, S., Dada, L., Dias, A., Duplissy, J., Finkenzeller, H., Garmash, O., He, X.-C., Hoyle, C. R., Kim, C., Kvashnin, A., Lehtipalo, K., Fischer, L., Molteni, U., Petäjä, T., Pospisilova, V., Quéléver, L. L. J., Rissanen, M., Simon, M., Tauber, C., Tomé, A., Wagner, A. C., Weitz, L., Volkamer, R., Winkler, P. M., Kirkby, J., Worsnop, D. R., Kulmala, M., Baltensperger, U., Dommen, J., El-Haddad, I., and Donahue, N. M.: Photo-oxidation of Aromatic Hydrocarbons Produces Low-Volatility Organic Compounds, Environ. Sci. Technol., 54, 7911–7921, https://doi.org/10.1021/acs.est.0c02100, 2020.

Wang, Y., Li, C., Zhang, Y., Li, Y., Yang, G., Yang, X., Wu, Y., Yao, L., Zhang, H., and Wang, L.: Secondary reactions of aromatics-derived oxygenated organic molecules lead to plentiful highly oxygenated organic molecules within an intraday OH exposure, Atmos. Chem. Phys., 24, 7961–7981, https://doi.org/10.5194/acp-24-7961-2024, 2024.

Yang, X., Ren, S., Wang, Y., Yang, G., Li, Y., Li, C., Wang, L., Yao, L., and Wang, L.: Volatility Parametrization of Low-Volatile Components of Ambient Organic Aerosols Based on Molecular Formulas, Environ. Sci. Technol., 57, 11595–11604, https://doi.org/10.1021/acs.est.3c02073, 2023.

Yao, L., Garmash, O., Bianchi, F., Zheng, J., Yan, C., Kontkanen, J., Junninen, H., Mazon, S. B., Ehn, M., Paasonen, P., Sipilä, M., Wang, M., Wang, X., Xiao, S., Chen, H., Lu, Y., Zhang, B., Wang, D., Fu, Q., Geng, F., Li, L., Wang, H., Qiao, L., Yang, X., Chen, J., Kerminen, V.-M., Petäjä, T., Worsnop, D. R., Kulmala, M., and Wang, L.: Atmospheric new particle formation from sulfuric acid and amines in a Chinese megacity, Science, 361, 278–281, https://doi.org/10.1126/science.aao4839, 2018.

Ye, Q., Wang, M., Hofbauer, V., Stolzenburg, D., Chen, D., Schervish, M., Vogel, A., Mauldin, R. L., Baalbaki, R., Brilke, S., Dada, L., Dias, A., Duplissy, J., Haddad, I. E., Finkenzeller, H., Fischer, L., He, X., Kim, C., Kürten, A., Lamkaddam, H., Lee, C. P., Lehtipalo, K., Leiminger, M., Manninen, H. E., Marten, R., Mentler, B., Partoll, E., Petäja, T., Rissanen, M., Schobesberger, S., Schuchmann, S., Simon, M., Tham, Y. J., Vazquez-Pufleau, M., Wagner, A. C., Wang, Y., Wu, Y., Xiao, M., Baltensperger, U., Curtius, J., Flagan, R., Kirkby, J., Kulmala, M., Volkamer, R., Winkler, P. M., Worsnop, D., and Donahue, N. M.: Molecular Composition and Volatility of Nucleated Particles from α-Pinene Oxidation between $-50\,^{\circ}C$ and $+25\,^{\circ}C$, Environ. Sci. Technol., 53, 12357–12365, https://doi.org/10.1021/acs.est.9b03265, 2019.

Zhang, X., Li, C., Xue, S., Yang, X., Wang, Y., Li, Y., Cai, R., Yao, L., and Wang, L.: Volatility Parametrization of Atmospheric Organic Compounds Based on Molecular Formula, ACS EST Air, 3, 291–301, https://doi.org/10.1021/acsestair.5c00167, 2026.

Zhang, Y., Wang, Y., Li, C., Li, Y., Yin, S., Claflin, M. S., Lerner, B. M., Worsnop, D., and Wang, L.: Interpretation of mass spectra by a Vocus proton-transfer-reaction mass spectrometer (PTR-MS) at an urban site: insights from gas chromatographic pre-separation, Atmos. Meas. Tech., 18, 3547–3568, https://doi.org/10.5194/amt-18-3547-2025, 2025.